RICE UNIVERSITY

Realization of the Bohr Atom

by

Brendan Wyker

A Thesis Submitted
in Partial Fulfillment of the
Requirements for the Degree

Master of Science

Approved, Thesis Committee:

F.B. Dunning, Advisor
Professor and Chair of Physics and
Astronomy

T.C. Killian
Associate Professor of Physics and
Astronomy

G. Fossati
Assistant Professor of Physics and
Astronomy

Houston, Texas

March, 2008

ProQuest LLC
789 E. Eisenhower Parkway
PO Box 1346
Ann Arbor, MI 48106-1346

Realization of the Bohr Atom

Brendan Wyker

Abstract

Localized wavepackets are created in high-n ($n \sim 300$) Rydberg atoms which travel in near-circular orbits around the nucleus. Application of carefully tailored electric fields to quasi-1D Rydberg atoms creates coherent superpositions of Stark states with near extreme values of one of the components of the angular momentum. Half-cycle electric field pulses (HCPs) probe the dynamics of the circular states producing signature oscillations in survival probability that correspond to the expected wavepacket evolution. Although these wavepackets slowly dephase and lose their localization, their motion can be followed for several orbits and provides an analog of the original Bohr model, i.e., an electron in circular classical orbit around the nucleus. Measurements of the asymmetry in survival probability with increasing probe strength at different phases of the orbit confirm orbital motion of the wavepacket. Classical trajectory Monte-Carlo simulations (CTMC) agree with experimental results, and provide promising leads for future studies.

Acknowledgments

First, I would like to thank my mother, Eileen, who passed away during the preparation of this thesis. She was an incredibly intelligent woman who would always talk over my head when I was a child, knowing that I would grow to catch up. I would also like to thank my wife, Margaret, for helping me through this difficult time, and for always being there for me. This work was guided by Dr. Barry Dunning, whose leadership and insight have been invaluable. My co-worker, Jeff Mestayer, has been an integral part of this experiment, and I would like to thank him for helping me transition to this experiment and the lab. The thoughtful and creative discussions of my other co-workers, Matt Cannon, Dean Neufeld, Jim Lancaster, Wei Zhao, Yi Liu, and Leonard Seuss have also been greatly appreciated. Thanks also to our collaborators on this project, Dr. Shuhei Yoshida, Dr. Carlos Reinhold, and Dr. Joachim Burgdörfer. I would be remissed if I were to forget my former co-workers in Maryland, Matthew Beeler, Emily Edwards, Scott Fletcher, Xianli Zhang, Tommy Willis, Francisco Elohim Becerra-Chavez, Adrian Perez Galvan, and all the others. Thanks also to Dr. Steve Rolston for all that he taught me during my time in Maryland. Finally, thanks to all of my friends and family that I don't have room to mention.

Contents

Figures

Chapter 1

Introduction

Rydberg atoms are defined as atoms with one or more electrons excited into a high-n state, where n represents the principal quantum number of the atom. Here, discussion will be limited to the case where only one electron, the valence electron of an alkali atom (potassium), is in an excited state. In terms of the classical Bohr theory the valence electron is excited to a high lying orbit of large radius. Unlike electrons in the Bohr theory, however, electrons in quantum theory are described by spatial electronic probability distributions, termed wavefunctions, which may or may not be well localized. In fact, the radial extent of the electronic distribution in a Rydberg atom does indeed increase rapidly with n, reaching a classical diameter $\sim$ 10 μm when $n = 306$. Table 1.1 outlines this dependence along with some of the more interesting characteristics of Rydberg atoms, with properties of the Hydrogen ground state, $n = 1$, given for comparison. Scaling equations are given in atomic units (see Sec. A.1), which are used throughout this text.

The term *circular state* has been used in the literature to describe Rydberg atoms with near extreme values of angular momentum [1–6]. Such atoms have potential applications in information processing, in cavity quantum electrodynamics, and in precision spectroscopy [7–11]. While these wavepackets can be produced with ra-

Table 1.1 : Scaling properties of Rydberg atoms.

Property	Scaling (a.u.)	$n = 1$	$n = 30$	$n = 306$
Mean Radius	n^2	5.3×10^{-9} cm	4.8×10^{-6} cm	5.0 μm
Orbital Period	$2\pi n^3$	1.5×10^{-4} ps	4.1 ps	4.3 ns
Binding Energy	$-1/2n^2$	13.6 eV	15 meV	145 μeV
Energy Spacing	$1/n^3$	10.2 eV	1.0 meV	0.94 μeV
Classical Field Ionization Threshold	$1/16n^4$	3.0×10^8 V/cm	400 V/cm	38 mV/cm

dial localization, localization in the angular coordinates has not been achieved [12]. Wavepackets, however, have been produced that are localized in both angular and radial coordinates [13,14], but these have been stationary wavepackets, generally with $\langle L \rangle \sim 0$. The present work is related to the engineering of wavepackets into states which are well localized, both radially and in their angular extent, that orbit the nucleus in well defined circular orbits, just as in the Bohr atom.

In the presence of electric fields the characteristics of Rydberg atoms can change quite drastically (see, for example, Ch. 2). One property of note is the effect of the electric field on the electron orbital angular momentum, which undergoes periodic

variations with an angular frequency

$$\omega_s = \frac{3}{2} n |\vec{F}|, \tag{1.1}$$

known as the Stark frequency [15]. This effect is used here to transform quasi one dimensional (quasi-1D) atoms, with $\langle L \rangle \sim 0$, into localized nonstationary circular states, $\langle L_i \rangle \sim \pm(n-1)$, by application of an electric field step of precise duration, $T_F = T_s/4 = \pi/2\omega_s$ [16]. The center of the wavepacket is expected to behave like a classical particle following a circular orbit,

$$\Big(x(t), z(t)\Big) \simeq \left(n^2 \cos\Big(-\frac{2\pi t}{T_n}\Big), n^2 \sin\Big(-\frac{2\pi t}{T_n}\Big)\right). \tag{1.2}$$

Similarly, the center of the wavepacket in momentum space will display strong periodic oscillations,

$$\Big(p_x(t), p_z(t)\Big) = \left(\frac{\mathrm{d}x}{\mathrm{d}t}, \frac{\mathrm{d}z}{\mathrm{d}t}\right) = \left(\frac{1}{n}\sin\Big(-\frac{2\pi t}{T_n}\Big), -\frac{1}{n}\cos\Big(-\frac{2\pi t}{T_n}\Big)\right), \tag{1.3}$$

90° out of phase.

In addition to the scaling of the mean radius of a Rydberg atom, the scaling of the classical orbital period, $T_n \sim n^3$, is also of note. Commercially available pulse generators are capable of producing half-cycle electric field pulses (HCPs) whose duration, T_p, can be much less than T_n for states with $n = 306$, as considered here. The term half-cycle pulse refers to an electric field pulse, $\vec{F}_{HCP}(t)$, whose profile is unidirectional. Such pulses, in the regime $T_p \ll T_n$, transfer impulsive momentum kicks to the electron given by [17]

$$\Delta\vec{p} = -\int \vec{F}_{HCP}(t)dt. \tag{1.4}$$

These kicks impart energy

$$\Delta E = \frac{\Delta \vec{p}^{\,2}}{2} + \vec{p_i} \cdot \Delta \vec{p}\,, \tag{1.5}$$

where $\vec{p_i}$ is the initial momentum of the excited electron. As classical ionization occurs for $E \geq 0$, Eq. 1.5 points out a means for probing the components and time evolution of the initial momentum of an electron based on measuring experimental survival probabilities as a function of kick strength, Δp, and its time of application. Evolution of the momentum of a nonstationary wavepacket is observed as an oscillation in survival probability.

Chapter 2 details some of the basic properties of Rydberg atoms, while elaborating on the theory of the techniques used in the production of nonstationary circular states. A discussion of the experimental apparatus is given in Chapter 3, where details of modifications made to the interaction region for this experiment are outlined. Experimental procedures and results are described in Chapter 4 followed by closing remarks in Chapter 5.

Chapter 2

Rydberg Basics

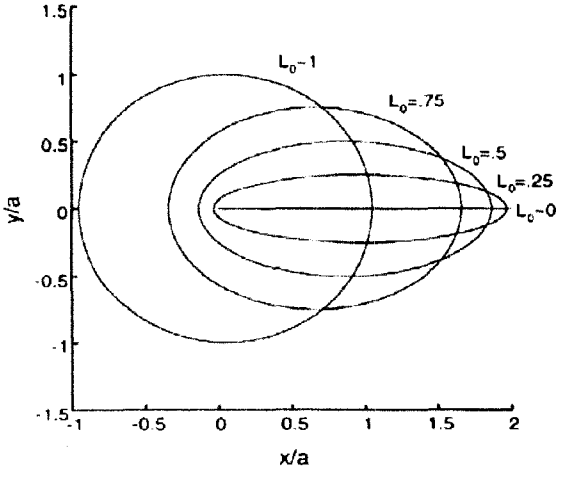

Figure 2.1 : Orbits of varying eccentricity. High L_0 implies near circular orbits, while low L_0 orbits are highly elliptical [18].

In the study of alkali Rydberg atoms it is useful to consider the properties of the hydrogen atom. Comparison may then be made between the hydrogenic and non-hydrogenic orbits. Rydberg electron dynamics are described to high accuracy using a classical model of Kepler orbits, modified where appropriate with quantum corrections. This viewpoint will be used in describing the relevant physical effects outlined in this chapter.

2.1 Orbital Equations

The single electron in a hydrogen atom experiences a potential of $V = -1/r$, where r denotes the separation of the electron from the nucleus. The resulting Hamiltonian in atomic units is then

$$H = \frac{\vec{p}^{\,2}}{2} - \frac{1}{r}, \tag{2.1}$$

where $\vec{p}$ denotes the momentum of the electron. For system energies $E < 0$, solutions of this Hamiltonian are closed elliptical or circular orbits in a plane, with conserved angular momentum, $\vec{L} = \vec{r} \times \vec{p}$. The eccentricity of the orbit is defined as $\varepsilon = \sqrt{1 - 2|E|L^2}$, and is related to the scaled, unitless angular momentum $L_0 = L\sqrt{2|E|} = \sqrt{1 - \varepsilon^2}$. As shown in Fig. 2.1, orbits with $L_0 \sim 0$ are highly elliptical, while orbits with $L_0 \sim 1$ are near circular orbits. The equation of an elliptical orbit in polar coordinates is given by [19]

$$r = \frac{L^2}{1 + \varepsilon \cos\theta}. \tag{2.2}$$

Another conserved quantity in the $1/r$ potential is the Runge-Lenz vector, $\vec{A}$, defined as

$$\vec{A} = \vec{p} \times \vec{L} - \hat{r}. \tag{2.3}$$

The magnitude of the Runge-Lenz vector in atomic units is the eccentricity, ε, of the orbit, while the direction is from the nucleus toward the point of closest approach (pericenter) of the orbit. Since $\vec{A} \cdot \vec{L} = 0$, the Runge-Lenz vector lies in the plane of the orbit, always perpendicular to $\vec{L}$.

Table 2.1 : Quantum defects of alkali atoms [20].

Atom	$\ell = 0$	$\ell = 1$	$\ell = 2$	$\ell = 3$
Li	0.40	0.04	0.00	0.00
Na	1.35	0.86	0.02	0.00
K	2.18	1.71	0.28	0.01
Rb	3.13	2.65	1.35	0.02
Cs	4.05	3.57	2.47	0.03

2.2 Quantum Defect

For highly elliptical orbits electrons in non-hydrogenic atoms penetrate the ionic core formed by the nucleus and core electrons. The resulting polarization of the core, as well as the change in effective potential due to the unshielded core, result in increased binding, and therefore decreased energy, of the Rydberg electron. To account for this an empirically determined quantum defect[1], δ_ℓ, is introduced, modifying the electron energy levels

$$E = \frac{-1}{2(n-\delta_\ell)^2}. \tag{2.4}$$

The quantum defect varies greatly with angular momentum, but is relatively insensitive to n. Table 2.1 shows quantum defects for some alkali-metal atoms. The potential experienced by the electron as it penetrates the core remains central in

[1] As the current work is semi-classical in nature, L, L_i, ℓ, and m have all been used in this text to describe angular momentum. These relate as $\langle L^2 \rangle = \ell(\ell+1)$ and $\langle L_i \rangle = m$, where L is the orbital angular momentum, and L_i is the component of the orbital angular momentum along the quantization axis. For a more detailed discussion see any elementary quantum mechanics text [21,22, for example].

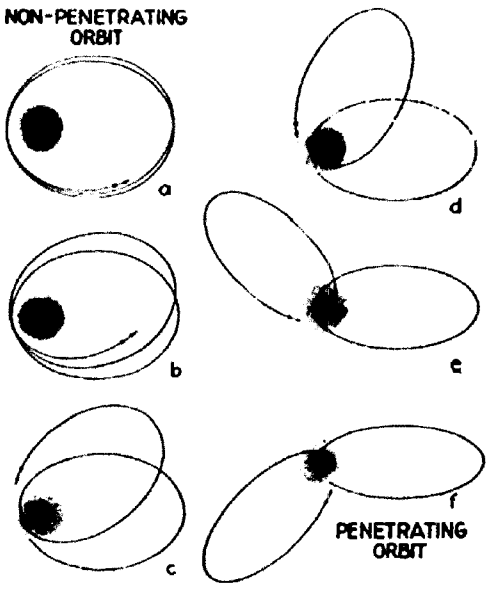

Figure 2.2 : Change of orbital precession with increasing core penetration for non-hydrogenic atoms [23].

character, meaning that the orbital angular momentum, $\vec{L}$, is still conserved. The Runge-Lenz vector, however, is no longer a conserved quantity [15]. As the angular momentum and energy determine the eccentricity, this leaves the direction of the Runge-Lenz vector as the quantity that varies. The resulting orbits retain their eccentricity, while the pericenter of the orbit precesses around the atom as shown in Fig. 2.2. Following the discussion of Ref. [24], an approximation of the precession frequency can be made. The high-n character of Rydberg atoms makes reasonable the assumption that $\delta_\ell \ll n$, leading to the approximation

$$E \approx -\frac{1}{2n^2} - \frac{\delta_\ell}{n^3}. \tag{2.5}$$

The classical precession frequency associated with neighboring ℓ states of the same n is then

$$\omega_\ell = \frac{\delta_\ell - \delta_{\ell+1}}{n^3}. \tag{2.6}$$

Treating ℓ as a semi-classical continuous variable we may write

$$\omega_\ell = -\frac{1}{n^3}\frac{\partial \delta_\ell}{\partial \ell} = -\omega_n \frac{\partial \delta_\ell}{\partial \ell}, \tag{2.7}$$

where ω_n is the classical orbital period. Retaining the dipole term of the multipole expansion of the core potential results in the Hamiltonian

$$H = H_{Coulomb} + \frac{\alpha_d}{2r^4}, \tag{2.8}$$

where $H_{Coulomb}$ is the pure Coulomb Hamiltonian and α_d is the dipole polarizability of the core. Relating Eq. 2.8 with Eq. 2.5 suggests that $\delta_\ell/n^3 = -\alpha_d/2r^4$. The radial dependence can be evaluated by averaging over a Kepler period,

$$\begin{aligned} \langle r^{-4} \rangle &= \frac{1}{2\pi n^3}\int_0^\tau r^{-4} \mathrm{d}t \\ &= \frac{\ell^{-5}}{2\pi n^3}\int_{-\pi}^{\pi}(1+\varepsilon\cos\theta)^2 \mathrm{d}\theta \\ &= \frac{\ell^{-5}}{n^3}(1+\varepsilon^2/2). \end{aligned} \tag{2.9}$$

As $\varepsilon = \sqrt{1-\frac{\ell^2}{n^2}}$, δ_ℓ may be written

$$\delta_\ell = \frac{3}{4}\alpha_d \ell^{-5}, \tag{2.10}$$

which, upon differentiation and rearrangement, gives a compact version of the precession due to the quantum defect as

$$\omega_\ell = \frac{5\delta_\ell}{n^3 \ell}. \tag{2.11}$$

2.3 Parabolic Coordinates[2]

To solve the Schrödinger equation describing the hydrogen atom in a field, $\vec{F}$, it is useful to transform to parabolic coordinates, (η, ξ, ϕ). Setting

$$\begin{aligned} \eta &= -z + \sqrt{x^2 + y^2 + z^2}, \\ \xi &= z + \sqrt{x^2 + y^2 + z^2}, \\ \phi &= \arctan \frac{y}{x}, \end{aligned} \tag{2.12}$$

or, equivalently

$$\begin{aligned} x &= \sqrt{\xi\eta} \cos\phi, \\ y &= \sqrt{\xi\eta} \sin\phi, \\ z &= \frac{\xi - \eta}{2}, \\ r &= \frac{\xi + \eta}{2}, \end{aligned} \tag{2.13}$$

the Schrödinger equation becomes

$$\left(-\frac{\nabla^2}{2} - \frac{2}{\xi + \eta} + \frac{F(\xi - \eta)}{2} \right) \Psi = E\Psi, \tag{2.14}$$

with

$$\nabla^2 = \frac{4}{\xi + \eta} \frac{\partial}{\partial \xi} \left(\xi \frac{\partial}{\partial \xi} \right) + \frac{4}{\xi + \eta} \frac{\partial}{\partial \eta} \left(\eta \frac{\partial}{\partial \eta} \right) + \frac{1}{\xi\eta} \frac{\partial^2}{\partial \phi^2}. \tag{2.15}$$

The coordinates ξ and η define confocal parabolas that are rotated about the z axis. $\xi = 0$ corresponds to the $-z$ axis, while $\eta = 0$ corresponds to the $+z$ axis. Figure 2.3 illustrates a 2D example of the parabolic coordinate system. Assuming a

[2] Much of the discussion in this section follows that of Gallagher [20].

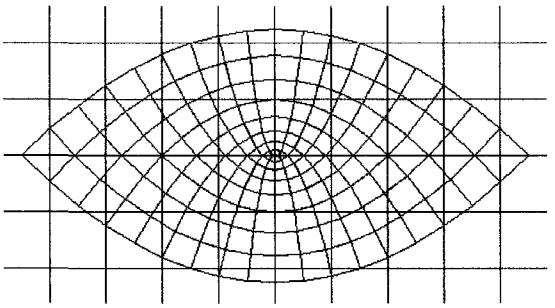

Figure 2.3 : A sample of the parabolic coordinate system. ξ represents downward facing parabolas, while η represents upward facing parabolas [25].

separable solution, $\Psi(\xi,\eta,\phi) = u_1(\xi)u_2(\eta)e^{\pm m\phi}$, yields

$$\begin{aligned}
\frac{d}{d\xi}\left(\xi\frac{du_1}{d\xi}\right) + \left(\frac{E\xi}{2} + Z_1 - \frac{m^2}{4\xi} - \frac{F\xi^2}{4}\right)u_1 = 0 \\
\frac{d}{d\eta}\left(\eta\frac{du_2}{d\eta}\right) + \left(\frac{E\eta}{2} + Z_2 - \frac{m^2}{4\eta} + \frac{F\eta^2}{4}\right)u_2 = 0,
\end{aligned} \tag{2.16}$$

where the separation constants Z_1 and Z_2 are related by $Z_1 + Z_2 = 1$. These constants are known as the effective charges binding the electrons in the ξ and η coordinates [20]. It is convention to solve this system in the zero field limit and use perturbation theory to determine the effects of the field on the solution. Quantum numbers n_1 and n_2 are introduced to describe the zero field hydrogenic parabolic states. These quantum numbers are not fully independent, following the relation

$$n = n_1 + n_2 + |m| + 1, \tag{2.17}$$

and determine the effective charges

$$\begin{aligned}
Z_1 &= \frac{1}{n}\left(n_1 + \frac{|m|+1}{2}\right), \\
Z_2 &= \frac{1}{n}\left(n_2 + \frac{|m|+1}{2}\right).
\end{aligned} \tag{2.18}$$

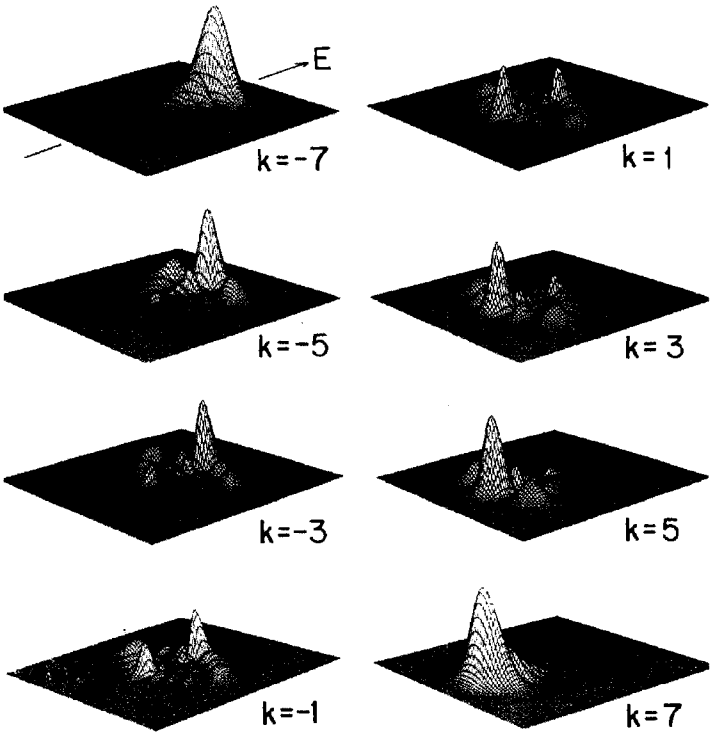

Figure 2.4 : Charge distribution for the parabolic eigenstates of H : $n = 8, m = 0, k = n_1 - n_2 = -7$ to $+7$. The asymmetry of the charge distribution for the extreme Stark states leads to a permanent dipole moment [20].

They also relate to the expectation value of a component of the Runge-Lenz vector,

$$\langle A_z \rangle = \frac{n_1 - n_2}{n} \equiv \frac{k}{n}. \tag{2.19}$$

Using the approximate form of the Laguerre polynomials an approximate, unnormalized wavefunction may be written [20]

$$\psi_{nn_1n_2m} \sim e^{im\phi} \xi^{n_1+|m|/2} \eta^{n_2+|m|/2} e^{-(\xi+\eta)/2n}. \tag{2.20}$$

Squaring the absolute value and reverting back to polar coordinates yields the elec-

tronic probability distribution [20]

$$|\psi_{nn_1n_2m}|^2 = r^{2n-2}(1+\cos\theta)^{2n_1+|m|}(1-\cos\theta)^{2n_2+|m|}e^{-2r/n}. \tag{2.21}$$

This distribution is illustrated in Fig. 2.4 for $n = 8$, $m = 0$, and $n_1 - n_2 = -7, \ldots, 7$.

2.4 Effect of a Static Electric Field

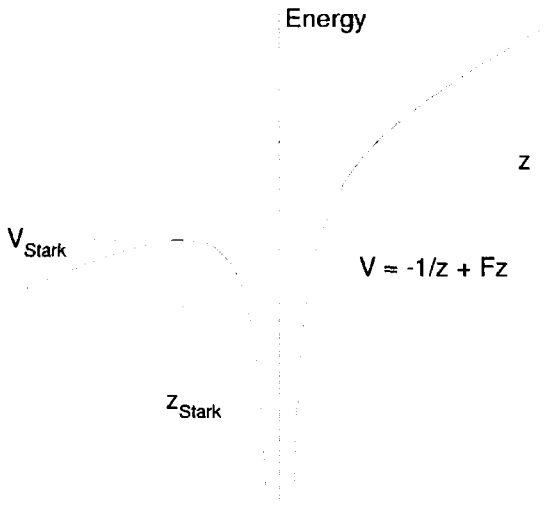

Figure 2.5 : Potential energy for an electron in a uniform, static electric field applied in the z direction.

The presence of external electric and magnetic fields will also cause changes in the electron orbit. When placed in a uniform, static electric field, F, oriented in the z direction, the potential experienced by the electron will be

$$V = -\frac{1}{r} + Fz. \tag{2.22}$$

Such a potential is illustrated in Fig. 2.5 where the presence of a saddle point on the z-axis is shown. The saddle point is located at $z_s = -1/\sqrt{F}$, with a potential of

$V = -2\sqrt{F}$. Classical ionization occurs above this barrier, at a threshold field of

$$F_{thresh} = \frac{E^2}{4} = \frac{1}{4}\frac{1}{(2n^2)^2} = \frac{1}{16n^4}, \tag{2.23}$$

as stated in Table 1.1. A portion of the kinetic energy of an electron with a nonzero component of angular momentum along the field axis goes into the momentum perpendicular to the field, thereby raising the field necessary to ionize the electron [26]. Labeling the angular momentum $\rho^2\dot{\theta} = L_z$ we may write the Hamiltonian in cylindrical polar coordinates (ρ, θ, z) as

$$H = \frac{p_\rho^2 + p_z^2}{2} + \frac{L_z^2}{2\rho^2} - \frac{1}{r} + Fz, \tag{2.24}$$

giving an effective potential energy

$$V_{eff} = \frac{m^2}{2\rho^2} - \frac{1}{r} + Fz, \tag{2.25}$$

which varies with m. For the case $m = 0$, this leaves the same threshold as before. The potential for states with $m \neq 0$ leads to an increase in the classical ionization threshold by [26]

$$\frac{\Delta F}{F_{thresh}} = \frac{|m|\sqrt{|E|}}{2} = \frac{|m|}{2n}. \tag{2.26}$$

The energy shift for an atom with an overall dipole moment, $\vec{d}$, in a field, $\vec{F}$ is

$$\Delta E = -\vec{d} \cdot \vec{F}. \tag{2.27}$$

This is not to be confused with the dipole term resulting from the polarizability of the core in Eq. 2.8. Averaged over a Kepler period the direction of the dipole moment will

point toward the pericenter of the orbit, $\hat{A}$. The magnitude of the dipole moment, averaged over the same period, relates to the magnitude of the average position, $|\langle\vec{d}\rangle| = |\langle\vec{r}\rangle|$. In spherical coordinates

$$\begin{aligned} |\langle\vec{d}\rangle| &= \frac{1}{\tau}\int_0^\tau r\cos\theta\,\mathrm{d}t \\ &= \frac{1}{2\pi n^3}\int_{-\pi}^{\pi} r\cos\theta\,\frac{1}{\dot{\theta}}\,\mathrm{d}\theta \\ &= \frac{1}{2\pi n^3}\int_{-\pi}^{\pi} \frac{r^3}{r^2\dot{\theta}}\cos\theta\,\mathrm{d}\theta \\ &= \frac{L^5}{2\pi n^3}\int_{-\pi}^{\pi} \frac{\cos\theta}{(1+\varepsilon\cos\theta)^3}\,\mathrm{d}\theta \\ &= \frac{3}{2}n^2\varepsilon. \end{aligned} \tag{2.28}$$

Eq. 2.2 and $r^2\dot{\theta} = L$ are used in the fourth line, and the definition of the eccentricity, $\varepsilon = \sqrt{1 - L^2/n^2}$, is used in the last line. Since $|\vec{A}| = \varepsilon$ the time averaged vector dipole moment is

$$\langle\vec{d}\rangle = \frac{3}{2}n^2\langle\vec{A}\rangle. \tag{2.29}$$

Casting the potential in parabolic coordinates,

$$V(\xi,\eta,\phi) = -\frac{2}{\xi+\eta} + \frac{F(\xi-\eta)}{2}, \tag{2.30}$$

it is possible to obtain a separable solution to the Schrödinger equation, even with the electric field, while this cannot be done in spherical coordinates. The energy levels are given to second order by [27]

$$E = -\frac{1}{2n^2} + \frac{3}{2}n(n_1-n_2)F - \frac{1}{16}n^4F^2[17n^2 - 3(n_1-n_2)^2 - 9m^2 + 19]. \tag{2.31}$$

The first term is recognized as the field-free hydrogen energy, while the second and third terms are the first and second order effects of the electric field. The second

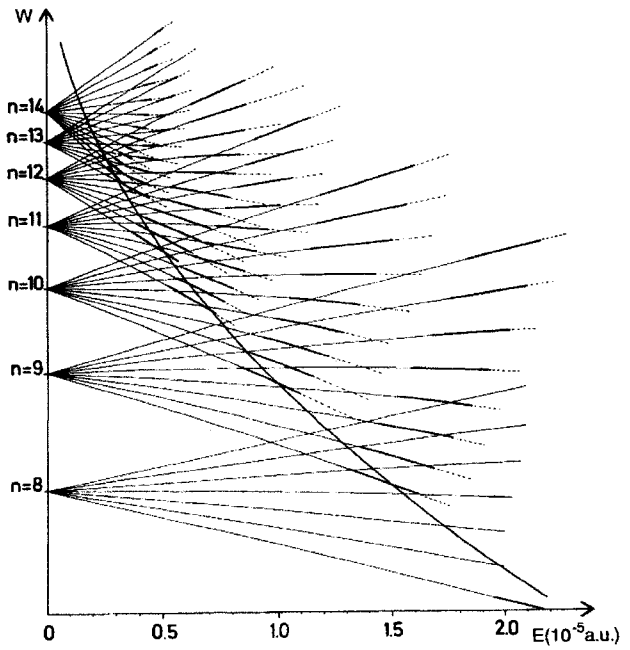

Figure 2.6 : Stark structure and field ionization properties of the $|m| = 1$ states of the H atom. Here the label W represents the energy E, while the label E represents the field F. The zero field manifolds are characterized by the principal quantum number n. The saddle point limit $E_c = -2\sqrt{F}$ is shown by a heavy curve. Field broadened Stark states appear approximately only for $E > E_c$ [20].

order term lifts the m degeneracy, while for circular states, $|m| = n - 1$, $n_1 = n_2 = 0$, the first order term vanishes. Figure 2.6 shows an example of the Stark energy level structure for the $|m| = 1$ states of hydrogen, where the effects of the electric field on the degenerate zero field energy states can be observed.

Focusing on the first order Stark correction we see an energy level splitting of $\Delta E = 3n(n_1 - n_2)F/2$. Notice that this energy shift is equivalent to that obtained considering the effect of an electric field on a dipole, Eqs. 2.27 and 2.29, and inserting Eq. 2.19. The first order separation between Stark energy levels (equivalent to a

frequency in atomic units) is called the Stark frequency, and is given by

$$\omega_s = \frac{3}{2} nF. \tag{2.32}$$

The presence of the electric field acts both to set a preferred quantization axis and to eliminate the spherical symmetry of the potential. The angular momentum is no longer conserved, and Hamilton's equations

$$\begin{aligned} \dot{\vec{p}} &= -\nabla H, \\ \dot{\vec{r}} &= \nabla_p H, \end{aligned} \tag{2.33}$$

where ∇_p denotes the derivatives with respect to momentum, describe the resulting dynamics. Writing the Hamiltonian as $H = H_{Coulomb} + V_F(\vec{r})$, where $H_{Coulomb}$ and $V_F(\vec{r})$ are the pure Coulomb Hamiltonian and electric field potential, respectively, the change in angular momentum becomes

$$\begin{aligned} \dot{\vec{L}} &= \dot{\vec{r}} \times \vec{p} + \vec{r} \times \dot{\vec{p}} \\ &= -\vec{r} \times [\nabla H_{Coulomb} + \nabla V_F(\vec{r})] \\ &= \dot{\vec{L}}_{Coulomb} - \vec{r} \times \nabla V_F(\vec{r}) \\ &= -\vec{r} \times \nabla V_F(\vec{r}) \\ &= -\vec{r} \times \vec{F}, \end{aligned} \tag{2.34}$$

where $L_{Coulomb}$ is the conserved angular momentum of the pure Coulomb potential, and the relation $\vec{F} = \nabla V_F(\vec{r})$ has been used in the last step. Time averaging over the

Kepler orbit yields

$$\begin{aligned}\langle\dot{\vec{L}}\rangle &= \langle-\vec{r}\times\vec{F}\rangle \\ &= -\langle\vec{r}\rangle\times\vec{F} = \langle\vec{d}\rangle\times\vec{F} \\ &= \frac{3}{2}n^2\langle\vec{A}\rangle\times\vec{F}. \end{aligned} \tag{2.35}$$

The Runge-Lenz vector evolves as

$$\begin{aligned}\dot{\vec{A}} &= \dot{\vec{p}}\times\vec{L}+\vec{p}\times\dot{\vec{L}}-\dot{\hat{r}} \\ &= [-\nabla H_{Coulomb}-\nabla V_F(\vec{r})]\times\vec{L}+\vec{p}\times\dot{\vec{L}}-\dot{\hat{r}} \\ &= (-\nabla H_{Coulomb}\times\vec{L}-\dot{\hat{r}})-\vec{F}\times\vec{L}+\vec{p}\times\dot{\vec{L}} \\ &= \dot{\vec{A}}_{Coulomb}-\vec{F}\times\vec{L}+\vec{p}\times\dot{\vec{L}} \\ &= -\vec{F}\times\vec{L}+\vec{p}\times\dot{\vec{L}}, \end{aligned} \tag{2.36}$$

where $\vec{A}_{Coulomb}$ is the conserved Coulombic Runge-Lenz vector. It is instructive to time average Eq. 2.36 by term. Expanding the second term

$$\begin{aligned}\vec{p}\times\dot{\vec{L}} &= \vec{p}\times(-\vec{r}\times\vec{F}) \\ &= -\vec{r}(\vec{p}\cdot\vec{F})+\vec{F}(\vec{p}\cdot\vec{r}), \end{aligned} \tag{2.37}$$

we see that $\vec{p}\cdot\vec{r}=\frac{1}{2}\frac{\mathrm{d}}{\mathrm{d}t}r^2$ will average to zero over an orbit as it is an exact differential of an even function. Another quantity that will average to zero over an orbit is the exact differential [15]

$$\frac{\mathrm{d}}{\mathrm{d}t}[\vec{r}(\vec{r}\cdot\vec{F})]=\vec{r}(\vec{p}\cdot\vec{F})+\vec{p}(\vec{r}\cdot\vec{F}), \tag{2.38}$$

which implies that $\langle \vec{r}(\vec{p}\cdot\vec{F})\rangle = -\langle \vec{p}(\vec{r}\cdot\vec{F})\rangle$. The triple product expansion of the first term in the last line of Eq. 2.36 is then

$$\begin{aligned} -\vec{F}\times\vec{L} &= -\vec{F}\times(\vec{r}\times\vec{p}) \\ &= -\vec{r}(\vec{p}\cdot\vec{F}) + \vec{p}(\vec{r}\cdot\vec{F}) \\ &= -2\vec{r}(\vec{p}\cdot\vec{F}). \end{aligned} \tag{2.39}$$

Leaving $\vec{F}\times\vec{L}$ as it is in Eq. 2.36 and combining Eqs. 2.37 and 2.39 yields a time averaged value for the change in the Runge-Lenz vector of

$$\langle \dot{\vec{A}}\rangle = \frac{3}{2}\langle \vec{L}\rangle \times \vec{F}. \tag{2.40}$$

Taking another derivative of Eq. 2.40 and plugging in Eq. 2.35 yields

$$\begin{aligned} \langle \ddot{\vec{A}}\rangle &= -\left(\frac{3}{2}n\right)^2[(\vec{F}\times\langle\vec{A}\rangle)\times\vec{F}] \\ &= -\left(\frac{3}{2}n\right)^2[\langle\vec{A}\rangle(\vec{F}\cdot\vec{F}) - \vec{F}(\vec{F}\cdot\langle\vec{A}\rangle)]. \end{aligned} \tag{2.41}$$

As F is in the z direction, $\langle \ddot{A}_z\rangle = 0$. The remaining components follow the equation

$$\langle \ddot{\vec{A}}\rangle = -\left(\frac{3}{2}nF\right)^2\langle\vec{A}\rangle, \tag{2.42}$$

which shows that the Runge-Lenz vector and, by similar analysis, the angular momentum rotate about the z axis at the Stark frequency, $\omega_s = 3nF/2$. The physical picture is that of a precessing ellipse, at ω_s, with an ellipticity that also varies at ω_s [15]. This second statement, that the ellipticity of the orbit can be controllably varied with a uniform, static electric field of precise duration, is one of the fundamental concepts in the production of the circular wavepackets discussed in this text.

2.5 Quasi-1D Atoms

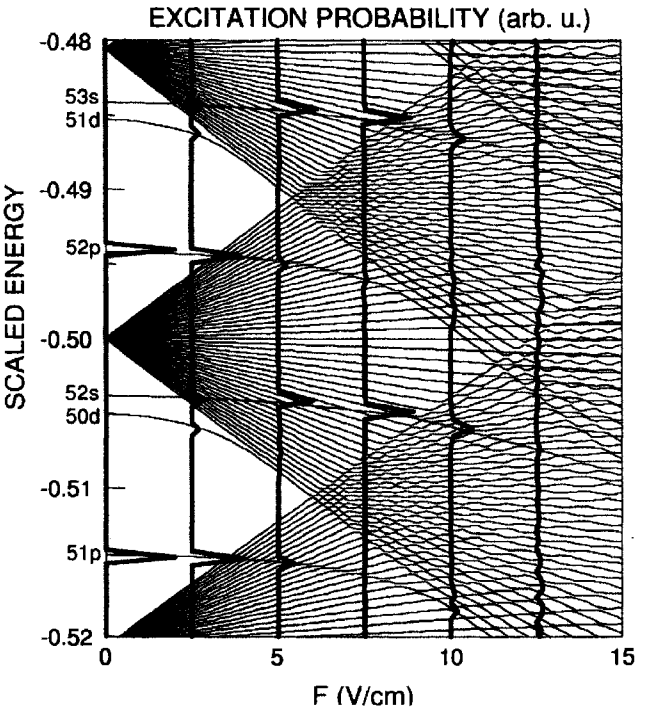

Figure 2.7 : Calculated Stark energy level structure for K($m = 0$) states in the vicinity of $n = 50$ (thin lines). Also included is the probability for photoexcitation from the ground state (thick lines) by a laser with a linewidth $\Delta\omega_L = 10^{-3}/n^2$ for different values of applied DC field. Energies are displayed in scaled units $\epsilon_0 = n^2\epsilon$ [14].

The production of strongly polarized, quasi-1D Rydberg atoms forms the first step in the process of creating localized nonstationary circular wavepackets. The extreme members of the high-n Stark manifolds have large permanent electric dipole moments and approximate quasi-1D states [14]. These states, however, have low excitation probabilities. In order to create the desired quasi-1D states, the coupling of Stark states is utilized. These $L_0 \sim 0$ wavepackets are produced by photoexciting

a thermal beam of potassium atoms in a weak dc electric field (see Sec. 3.3). The calculated Stark energy level structure for $n \sim 50$, is shown in Fig. 2.7. Though the work in this text takes place at $n = 306$, the figure is shown for $n = 50$, as at higher n it becomes difficult to resolve the energy levels graphically. The quantum defects that determine the structure, however, are relatively independent of n, allowing a qualitative understanding of the features of the Stark energy level structure.

Photoexcitation probabilities calculated for vertically polarized incident radiation, exciting potassium from the $4s$ ground state, for several values of applied dc field are superimposed on the figure. Dipole coupling dictates that transitions obey the selection rule $\langle n'\ell'|z|n\ell\rangle \sim \delta_{\ell,\ell\pm1}$, where primed quantum numbers represent final states, the unprimed quantum numbers represent the initial $4s$ ground state, and $\delta_{i,j}$ is the Kronecker delta. In zero field, then, only the p state is excited. As the electric field is increased, however, Stark states that adiabatically correlate to non-p states (such as the levels that trace to the $50d$ and $51d$ states in the figure), take on p state character, in that the Stark state expansion in terms of the zero field states

$$|\alpha\rangle = \sum_{n,\ell} a_{n,\ell}|n,\ell\rangle, \tag{2.43}$$

contains non-zero contributions from the zero field p states, i.e., there exists an $a_{n,\ell=1} \neq 0$. In Eq. 2.43 $|\alpha\rangle$ denotes the Stark state, expanded in terms of the $|n,\ell\rangle$ zero field basis states, with proportionality coefficients $a_{n,\ell}$.

As detailed in Table 2.1, while the s and p states have large quantum defects, the d state quantum defect of potassium is ≈ 0.28. As the electric field is increased the

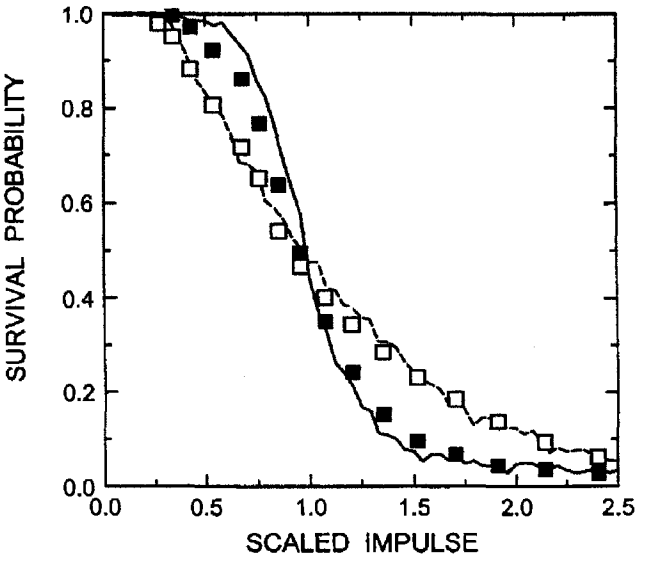

Figure 2.8 : Survival probabilities for quasi-1D atoms in low lying states in the $n = 350$ manifold as a function of scaled momentum. Closed squares represent experimental data for HCPs applied transverse to the axis of the atom, while open squares represent data for HCPs applied along the axis. Lines represent CTMC simulations [28].

levels that begin as s and p states first encounter states in manifolds of different n. The d levels, due to their small quantum defect, first encounter states in the manifold of the same n. This is seen in Fig. 2.7 as the $50d$ state approaches the manifold originating at $\epsilon = -0.50$ in the zero field limit, while the $n = 50$ manifold encounters the $52s$ and $52p$ states first. Coupling is strongest between levels of the same n [14], leading to strong mixing of the d state with the extreme states of the neighboring manifold as the field is increased to ~ 2.5 V/cm in Fig. 2.7.

Production of quasi-1D states can be verified using HCPs. Recalling Eq. 1.5 it is evident that the application of HCPs of duration $T_p \ll T_n$ parallel to the initial momentum will increase the electron energy, while HCPs applied anti-parallel will

tend to decrease the energy, leading to ionization only for kicks $|\Delta p| > 2p_z$. A slow decrease in survival probability is then expected as the magnitude of HCPs directed parallel to the axis of a quasi-1D atom is increased. HCPs directed transverse to the axis of a quasi-1D atom, however, should lead to a narrow distribution of energy transfers, $\Delta E \sim \Delta p^2/2$, resulting in a sharp drop in survival probability beyond a threshold impulse, $|\Delta\vec{p}| = \sqrt{2|E|}$, or in scaled quantities $\Delta\vec{p}_0 = 1$. This behavior has been demonstrated experimentally [28] for states near $n = 350$, and is illustrated in Fig. 2.8.

In the present work, at $n = 306$, quasi-1D atoms are photoexcited in a weak ~ 500 μV/cm dc field. Field steps of -20 mV/cm are then applied transverse to the quasi-1D axis for $T_F = T_s/4 = \pi/2\omega_s$ to produce localized circular states. Details of the excitation scheme and experimental procedure are laid out in Chapter 4, where the results of simulations and the corresponding experimental results are also discussed.

Chapter 3

The Experimental Apparatus

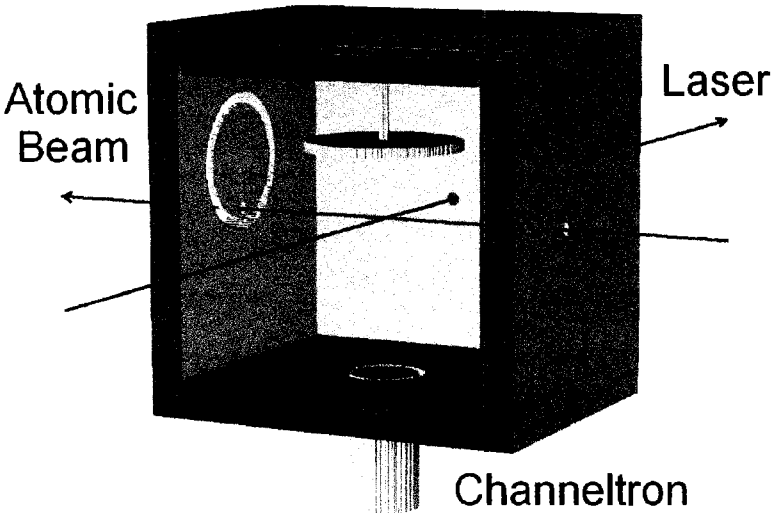

Figure 3.1 : Diagram of the modified apparatus with the front face removed for illustrative purposes. A UV laser pulse intersects a collimated alkali beam exciting high-n Rydberg states. Half-cycle electric field pulses (HCPs) and electric field steps are applied by the two electrodes, while the channeltron electron multiplier measures electrons resulting from field ionization.

The present experimental apparatus is a slight modification of that used with much success in previous studies of Rydberg atoms [29, 30]. This comprises three pairs of copper plate electrodes arranged as a cube, the interaction region, whose faces are electrically isolated so they may be individually biased to reduce residual electric fields in the interaction region to $\lesssim 50\,\mu$V/cm. Two electrodes are also incorporated for

the application of field steps and HCPs, along with a channeltron electron multiplier for the detection of field-ionized electrons.

High-n Rydberg atoms are produced in the interaction region via single photon excitation with a frequency doubled Coherent 699-21 CW Rhodamine 6G (Rh6G) dye laser whose output is chopped by an acousto-optic modulator into a train of $1\,\mu$s duration pulses. The laser is focused into the center of the interaction region where it intersects a thermal potassium beam originating from a potassium beam oven. Following excitation, the Rydberg atoms are subject to one or more carefully tailored electric field pulses. Surviving Rydberg atoms are measured by application of a field ionization pulse, after some delay, and the resulting electrons are detected by a channeltron electron multiplier. Measurements with no HCPs applied are repeated at routine intervals to determine the number of Rydberg atoms initially created and obtain survival probabilities. Due to the low probability of Rydberg excitation during a given cycle, data are accumulated following many cycles to improve the statistics. Experiments are repeated approximately every $50\,\mu$s.

In order to study the circular states of interest it is necessary to probe in at least two dimensions. For this reason one of the faces of the cube was modified to allow for a side electrode (Fig. 3.1). The structure and placement of this electrode are described in Section 3.3, along with further details of the interaction region. A brief discussion of the general apparatus is laid out in Sections 3.1 & 3.2, while detection methods are described in Section 3.4. Finally, the creation of the necessary electric

field pulses, and how they couple into the system, are described in Section 3.5.

3.1 The Vacuum Chamber

The vacuum chamber consists of two stainless steel sections coupled by a 0.7 mm aperture. An initial vacuum on the order of 10 mTorr is produced by a Welch Duo Seal mechanical backing pump. Next, a vacuum of 5×10^{-8} Torr is produced using Varian VHS-6 and VHS-4 diffusion pumps. Bayard-Alpert ionization gages are located in each chamber to monitor pressure.

The source chamber houses the potassium beam oven and is pumped by the 4" diffusion pump. The oven contains a 5 g ampule of potassium. The body of the oven is heated to 315 °C by applying current to resistive heater cartridges inserted into the oven body. Heater cartridges are also placed in the nose of the oven which is heated to 365 °C; the temperature difference is maintained in order to prevent potassium from condensing on, and thereby clogging, the nose aperture. Thermocouples placed on the nose and body of the oven relay temperature information to a set of Omega CN9000A microprocessor temperature controllers which regulate the current applied to the heater cartridges.

Thermal radiation transfer from the oven to the rest of the apparatus is reduced through the use of heat shielding and water cooling. An aluminum heat shield surrounds the oven, reducing heat transfer and containing excess potassium vapor. The oven and heat shield are further surrounded by a copper enclosure, to which copper

tubing has been blazed. Chilled water is routed by vacuum feed-throughs into the copper tubing.

Potassium exits the oven through a 0.38 mm aperture in the nose and travels approximately 10 cm before passing through the 0.7 mm aperture which leads to the main chamber. A rough estimate of the beam's angular divergence may then be calculated using the expression

$$\theta_d = 2arctan\Big(\frac{d_f - d_i}{2l}\Big), \tag{3.1}$$

where θ_d denotes the angular divergence, d_f and d_i denote the diameters of the two apertures, and l denotes the distance between the apertures. With the values given the angular divergence is estimated to be $\sim 0.2°$.

The velocity distribution of the beam is estimated using [31]

$$f_{Beam}(v) = \frac{1}{2}\Big(\frac{m}{k_b T}\Big)^2 v^3 e^{-\frac{mv^2}{2k_b T}}, \tag{3.2}$$

where f_{Beam} is the Maxwell-Boltzmann velocity distribution of a beam. The first moment of the velocity distribution, $\langle v^n \rangle = \int v^n f(v)\, \mathrm{d}^3 v$ with $n = 1$, yields an average velocity of

$$\overline{v} = \sqrt{\frac{9\pi k_b T}{8m}}, \tag{3.3}$$

which, with the values given above, is $\overline{v} = 660$ m/s. Further characterization of the beam will be described as needed throughout the text.

The main chamber houses the interaction region (discussed in detail in Sec. 3.3) and is pumped by the 6" diffusion pump. Stray magnetic fields in the chamber

are reduced by μ-metal shielding to values $\leq$ 20 mG. Laser light enters and exits the chamber through quartz windows set at Brewster's angle, preferentially passing vertically polarized light. All electrical signals are routed through the chamber using semi-rigid coaxial copper cables.

3.2 The Laser System

Essential to the creation of Rydberg atoms is precise control of the excitation laser system, an extracavity doubled CR-699-21 Rh6G dye laser. A Coherent Verdi V8 laser is used to pump this laser. Rh6G laser dye, dissolved in ethelyne glycol, acts as the lasing medium yielding approximately 1 W of laser radiation over a tunable wavelength range of 570 – 610 nm. A Spectra-Physics Wavetrain frequency doubler is used to produce the near UV laser radiation needed for single photon Rydberg excitation.

The Verdi is a diode pumped solid state laser which reliably provides powerful and stable 532 nm pumping radiation, with a linewidth of 5 MHz and $< 0.03\,\%$ rms noise. The 7.5 W pump beam is focused into a jet of Rh6G flowing at approximately 10 m/s, expanding from a stainless steel nozzle into a flat laminar stream whose face is oriented at Brewster's angle to the incoming pump beam in order to minimize reflection loss [32]. A 380 GHz bandwidth birefringent filter, a 225 GHz free spectral range (FSR) thin etalon, and a 10 GHz FSR thick etalon combine to produce single frequency operation. The efficiency of single frequency operation is enhanced

through the use of a polarization rotating element referred to as an optical diode. This component ensures unidirectional operation through the use of optical activity and the Faraday effect, by slightly rotating the polarization of waves traveling in one direction, while leaving unchanged the polarization of waves traveling in the other direction [33]. Reflection losses at an intracavity Brewster plate then suppress the propagation of the unwanted traveling wave.

A portion of the CR-699 output beam is split off for use in active stabilization. Two detectors compare the intensities of an unmodified beam and one that passes through an oven stabilized Fabry-Perot interferometer containing a galvo driven Brewster plate, collectively known as the reference cavity. The interferometer output intensity varies with laser frequency providing the means to produce an error signal that is fed into the controls for varying the position of the intracavity Brewster plate and a piezoelectric-mounted cavity mirror. The position of the galvo driven Brewster plate, in the reference cavity, can be externally controlled allowing for a linear 30 GHz frequency scan. Active stabilization of the CR-699 maintains a linewidth of ≤ 500 kHz with a long term frequency drift of ≤ 50 MHz per hour.

Long-term stability is enhanced to ≤ 1 MHz per day by the Superlock system [34]. Another small portion of the CR-699 output is superposed with an orthogonally polarized beam from an Aerotech 110SF frequency stabilized Helium-Neon laser (HeNe). This combination is directed into a Burleigh confocal scanning Fabry-Perot etalon with a FSR of 750 MHz, controlled by a Burleigh RC45 etalon controller. A piezoelec-

tric transducer (PZT) scans one of the mirrors of the etalon leading to transmission peaks related to each laser's frequency. After passing through the etalon each beam is separately directed into a pair of photodiodes. Given a linear PZT response, the separation of a HeNe intensity peak from that of a CR-699 peak should be constant while the CR-699 is in a stable state. The PZT scan voltage at the time of each intensity peak is stored by a *sample and hold* circuit and the difference of the two values is compared to a reference voltage producing an error signal that is fed into the CR-699 control circuitry. Setting the reference voltage to a linear ramp enables frequency scans over a range of 800 MHz, while setting the reference voltage to a constant value allows for precise frequency locking. A scanning Michelson interferometer monitors the overall CR-699 wavelength [35].

The 1 W output of the CR-699 is then directed into the Wavetrain frequency doubler [36] producing, typically, $50 - 100$ mW of the near UV light needed for Rydberg excitation. A beta barium borate (BBO) crystal located in one arm of a triangular ring resonator is used as the nonlinear medium for second harmonic generation (SHG). Two curved mirrors and a PZT-mounted prism act as the vertices of the resonator. Phase matching, where the phase velocity of the harmonic wave matches that of the fundamental wave in the nonlinear material, is necessary in order to maximize conversion efficiency. This is achieved through the use of the birefringence of the BBO crystal, in that the angular dependence of the refractive index of the crystal may be used to match the phases of the waves by varying their incident angles with the aid

of the PZT-mounted prism. Optics located in between the CR-699 and the Wavetrain are used in the active resonator stabilization of the system. The Pound-Drever Hall [37] method is utilized by passing the incoming beam through an electro-optic modulator (EOM) and monitoring the superposition of signals with a photodiode. The EOM, driven by an electrical radio frequency (rf) signal, adds sidebands to the incident beam. A portion of the incident beam reflects off the resonator input mirror and interferes with a transmitted portion of the beam in the cavity. The rf modulation on the resulting beam is then measured by the photodiode. A double balanced mixer is used in the phase sensitive detection of the photodiode signal to produce the error signal used for active stabilization. The linewidth of the cavity is small enough that the rf sidebands are not transmitted into the cavity.

An Intra-Action acousto-optic modulator (AOM) then chops the beam into $1\,\mu$s pulses approximately every $50\,\mu$s. To do this the first order diffracted beam from the AOM, driven at a constant frequency, is kept while all other order beams are blocked. While the maximum intensity in the first order is less than that available in the zeroth order, a full extinction ratio is possible with the former while this is not possible with the latter. Steering mirrors then direct the beam through a lens and into the interaction region via a Brewster window.

3.3 The Interaction Region

Three pairs of planar copper plate electrodes, 10 cm × 10 cm, comprise the basic structure of the interaction region (IR) as illustrated in Fig. 3.1. The separation of these large plates from the center of the IR helps to reduce the effect of patch fields caused by nonuniformities in the plate electrode surfaces, while bias potentials applied to these plates reduce stray electric fields near the center of the IR to $\lesssim 50\,\mu$V/cm [29]. Vertical plate pairs are biased with a *push-pull* system where each plate is given an equal but opposite bias potential. The top and bottom plates, however, are arranged with the top plate receiving the full bias potential while the bottom plate is held at a constant potential. This is due to the location of the channeltron electron multiplier below the IR, which is accessed via a 1" diameter aperture in the bottom plate electrode covered by a fine copper mesh. More on this arrangement and the channeltron will be discussed in Sec. 3.4. A set of $0.1\,\mu$F capacitors connects the side plates to ground, thereby eliminating pickup of nearby rf signals by providing an rf-shunt. Apertures are located in the center of the four side walls to allow for the entrance and exit of the laser and the alkali atom beams. These beams cross, perpendicularly, in the center of the IR exciting high-n Rydberg states.

Hanging from the top plate of the IR is a 2" diameter, $\frac{1}{4}$" thick disk electrode. This electrode shares the bias of the top plate while independently receiving electric field pulses, and is held in place, 1" above the center of the IR, by a semi-rigid copper coaxial cable. A $50\,\Omega$ resistor connects the electrode to the coax shield to minimize

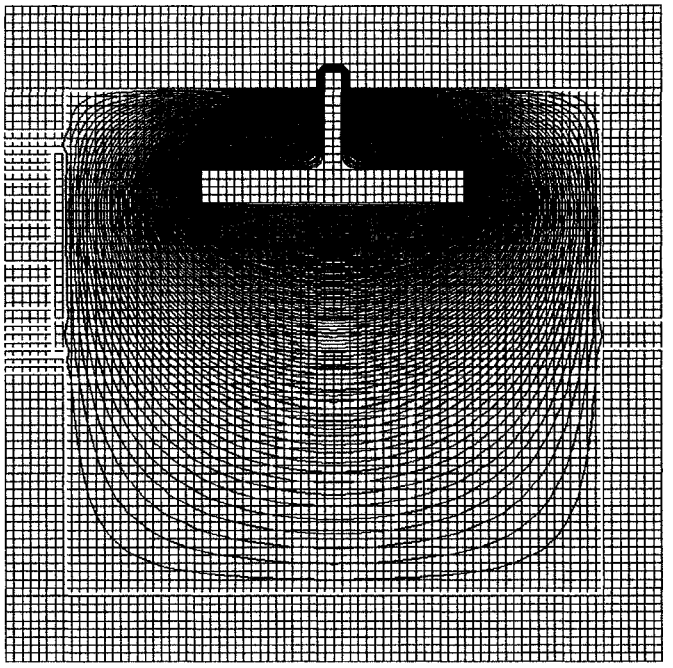

Figure 3.2 : A cross section of the IR with potential contours produced by applying an arbitrary potential to the top electrode while keeping all other surfaces grounded. Ninety contours are drawn equally spaced in potential from ground to the arbitrary potential applied on the top electrode.

reflections while allowing pulse rise times as fast as 200 ps. Figure 3.2 shows the potential contours that result when a static potential is applied to the top electrode while keeping all other electrodes grounded. Of note are the spacing and relative flatness of the contours in the vicinity of the center of the IR. These relate directly to the uniformity and direction, respectively, of the applied electric fields in the area via

$$\vec{F} = -\nabla\phi, \tag{3.4}$$

where $\vec{F}$ is the electric field and ϕ is the potential.

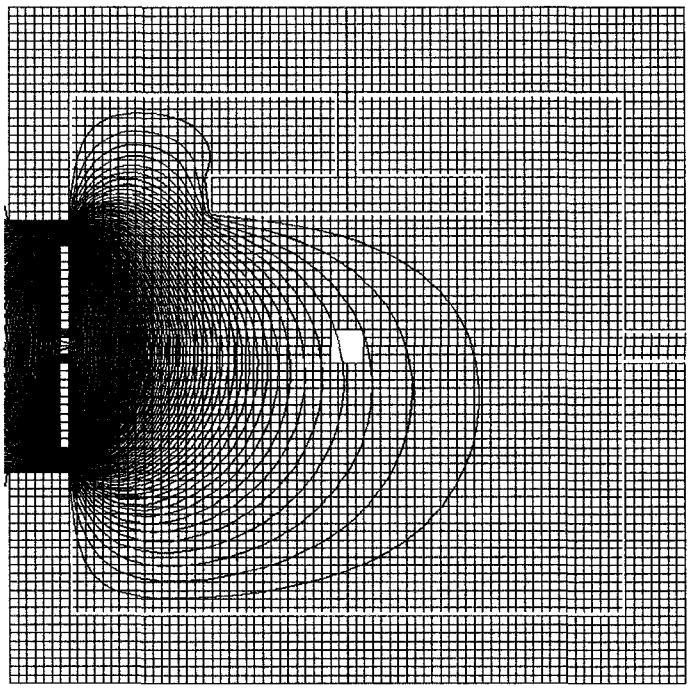

Figure 3.3 : A cross section of the IR with potential contours produced by applying an arbitrary potential to a centered side electrode while keeping all other surfaces grounded.

The two dimensional kicking necessary for the production of circular states requires the presence of a side electrode in the IR. This electrode shares the bias of the surrounding side plate while independently receiving electric field pulses. As with the top electrode, the uniformity and direction of the electric field produced by this electrode are important parameters. Other parameters that must also be satisfied are that the magnitude of the electric field produced be sufficient to produce the circular states and that the capacitance of the electrode, with respect to the large plate electrode it is near, be small enough to allow fast rise times for pulsed electric fields.

The electric field produced by the side electrode should point horizontally so as to be perpendicular to the direction of fields produced by the top electrode. The placement and size of the top electrode, however, complicate the placement of the side electrode as its presence modifies the resulting potential contours. Figure 3.3 shows the potential contours that result when a potential is applied to a centered side electrode. As is evident in the figure, the electric field near the center of the IR that would result from this arrangement is not directed horizontally. Numerical calculations show a deviation of approximately 14°. Recognizing the relation to minimal surfaces it be-

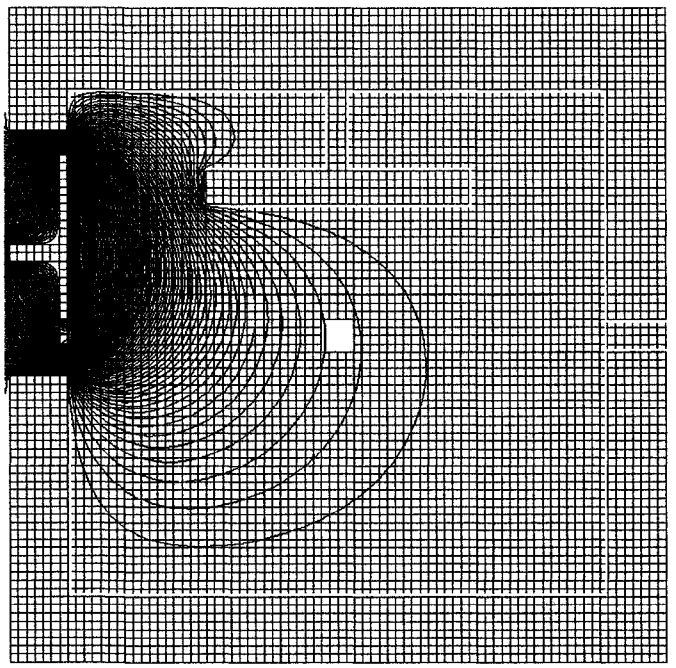

Figure 3.4 : A cross section of the IR with potential contours produced by applying an arbitrary potential to a side electrode, displaced upward from the center, while keeping all other surfaces grounded.

comes evident that in order to direct the electric field horizontally the side electrode must be relocated upward. Moving the electrode upward, however, moves it further away from the IR center thereby reducing the maximum attainable electric field for a given applied potential. While centered the side electrode is capable of producing a field strength 11% that of the top electrode. Numerical calculations were used to determine a reasonable compromise of field direction and strength resulting in a displacement of the side electrode upward by $\frac{5}{8}$", resulting in a field strength of 8% that of the top electrode and a field tipping of 3.6 °. Figure 3.4 shows the potential contours that result when a static potential is applied to the displaced side electrode while all other surfaces are held at ground.

The capacitance of the side electrode with respect to the surrounding plate electrode is roughly approximated using the parallel plate equation

$$C = \epsilon_o \frac{A}{d}, \tag{3.5}$$

where ϵ_o is the vacuum permittivity, A is the area of the edge of the side electrode, and d is the distance from the side electrode to the surrounding plate electrode. Here, $d = 3.18\,\text{mm}$, while the electrode radius is 19.1 mm, with an electrode thickness of 1.59 mm, yielding a side area of $190\,\text{mm}^2$, and a capacitance approximately $C = 0.5\,\text{pF}$. Just as with the top electrode, the side electrode has a $50\,\Omega$ resistor connecting it to the coax shield. This arrangement allows for pulse rise times around $\tau = RC = 25\,\text{ps}$. Having met all the requirements in theory, the side electrode was added to the apparatus yielding results to be described in Chapter 4.

3.4 Detection

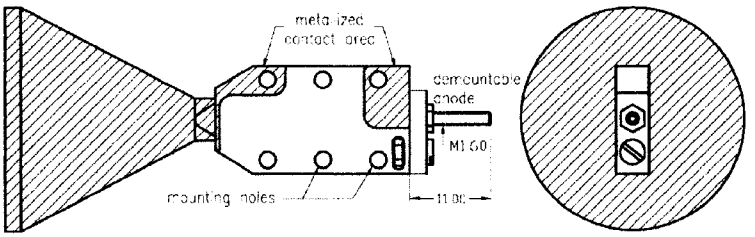

Figure 3.5 : Sjuts Optotechnik KBL 25RS channeltron electron multiplier schematic. The channeltron is used to detect electrons resulting from Rydberg atom ionization.

A 1" aperture is located in the center of the bottom plate electrode, covered by a series of fine mesh copper grids. Directly below these grids lies a Sjuts Optotechnik KBL 25RS channeltron channel electron multiplier (Fig. 3.5). To detect surviving Rydberg atoms a voltage ramp which rises from 0 to 5 V over a period of 5 μs is applied to the bottom plate, accelerating electrons into the funnel shaped aperture and curved channel of the channeltron. There, collisions with a hydrogen-reduced lead oxide glass lining produce an avalanche of secondary electron emissions. With a bias across the channeltron of 3 kV, up to 10^8 electrons can be produced from this process [38] which, upon collection by the anode, trigger an output pulse to a LeCroy MVL 100 amplifier/comparator. The MVL acts as a discriminator and amplifier reducing the number of spurious counts and improving the signal to noise ratio. The MVL outputs to an Ortec 566 time to amplitude converter (TAC) whose output ranges from 0 to 10 V based on the duration from the beginning of the ramp to the

time of the MVL signal. An analog to digital converter then passes the result to the computer for processing.

Though Rydberg ionization is a complex process, whose details may be found elsewhere [20,39, for example], Rydberg atom binding energies scale roughly as $-1/2n^2$, while classical ionization thresholds scale as $1/16n^4$. With a linear field ramp the above-mentioned technique allows for time sensitive, and therefore field sensitive, detection. This method forms the means of Selective Field Ionization (SFI), where the state of a Rydberg atom can be determined based on the field required for ionization. For the present study, however, it is sufficient to take the total number of ionized electrons, regardless of arrival time, since specific parent state information is not critical.

Previous work on the apparatus [18] shows that the low energy electrons produced by photoionization during the UV Rydberg excitation pulse, and by the applied HCPs, might remain in the IR for up to $5\,\mu$s. Thus, in order to obtain accurate survival probabilities the field ramp is applied $6\,\mu$s after the UV Rydberg excitation pulse, and the TAC start pulse is slightly delayed from the start of the field ramp. This way any free electrons from the initial Rydberg excitation, or those produced during the course of the experiment, are not counted in the determination of the overall survival probabilities. As stated before, the experimental cycle is repeated approximately every $50\,\mu$s. Experimental runs, during which HCPs and field steps are applied to the atoms, alternate with calibration runs, during which no HCPs are applied, in order to

determine survival probabilities. Due to the low Rydberg excitation probability of a given cycle, data from many cycles are accumulated to produce meaningful statistics.

3.5 Electric Field Pulses

The electric field steps and HCPs are produced using a pair of high speed pulse generators. The Hewlett Packard 8131A pulse generator is used for the field steps. This generator is capable of producing up to 5 V pulses with rise times < 200 ps. A Picosecond Pulse Labs 10,050A pulse generator is used for the production of HCPs and ionizing field steps. This generator is capable of 45 ps rise times and pulses up to 10 V over a duration of 100 ps to 10 ns. These pulse generators are triggered by a Stanford Research Systems DG535 Digital Delay Generator with up to 5 ps resolution.

Pulse strengths are adjusted through the use of fixed and rotary attenuators. Potential to field conversion is determined experimentally by varying the signal strength of short ($T_p \ll T_n$) HCPs while monitoring Rydberg atom survival probabilities. The potential required for 50% ionization has been shown [17] to correspond to a scaled momentum transfer of $\Delta p_0 = n^{-1}$ (see A.2) in this limit.

Chapter 4

Producing Localized Circular Wavepackets

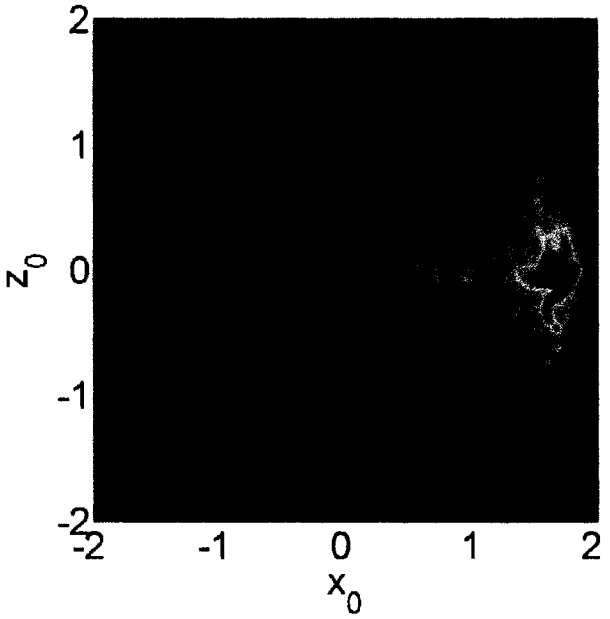

Figure 4.1 : Simulated initial quasi-1D distribution. CTMC simulations produce a representative spatial distribution for a wavepacket with a scaled dipole of 1.25.

With an understanding of the physical processes involved and the experimental apparatus available, the details of the creation and behavior of localized nonstationary circular wavepackets are discussed. As noted previously, in the present protocol potassium atoms are first photoexcited by a linearly polarized, near UV laser pulse to $n = 306$. The excitation takes place in the presence of a weak dc electric field directed

along the x-axis, $F_{dc}^{(x)} = 500\ \mu$V/cm, producing the initial quasi-1D state. Figure 4.1 shows the calculated spatial distribution associated with the initial quasi-1D state. Next, an electric field step is suddenly applied perpendicular to the quasi-1D state, namely, along the z axis. The rise and fall times of this field step were chosen to be ~ 0.3 ns. Equation 2.35, $\langle \dot{\vec{L}} \rangle = 3n^2 \langle \vec{A} \rangle \times \vec{F}/2$, describes the change in the angular momentum. Initially, $\langle \vec{A} \rangle$ points along the $-x$ axis, as this is the direction of the dipole moment of the quasi-1D atom. For an electric field step applied in the $-z$ direction the y component of the angular momentum initially increases negatively, i.e., the orbital motion becomes counterclockwise in the xz plane as shown in Fig. 4.2. The next section discusses the use of CTMC simulations to understand the dynamics involved in circular wavepacket creation, while Sec. 4.2 details the experimental results obtained using the present protocol.

4.1 Classical Trajectory Monte Carlo Simulation Results

Figure 4.2 shows the effect of a -20 mV/cm field step on the orbit and angular momentum distribution of a quasi-1D wavepacket. The upper portion of the figure illustrates the change in eccentricity of an orbit over time $T_s/2$, while the inset displays the evolution of the angular momentum distribution with time. Note that the initial, $L_y \sim 0$, state evolves into a high angular momentum state, $|L_y| \sim 300$, over a time $T_s/4 \approx 22$ ns, and returns to $L_y \sim 0$ at time $T_s/2 \approx 43$ ns. The goal, then, is to apply the field step just long enough for $|L_y|$ to reach its maximum, and then to quickly

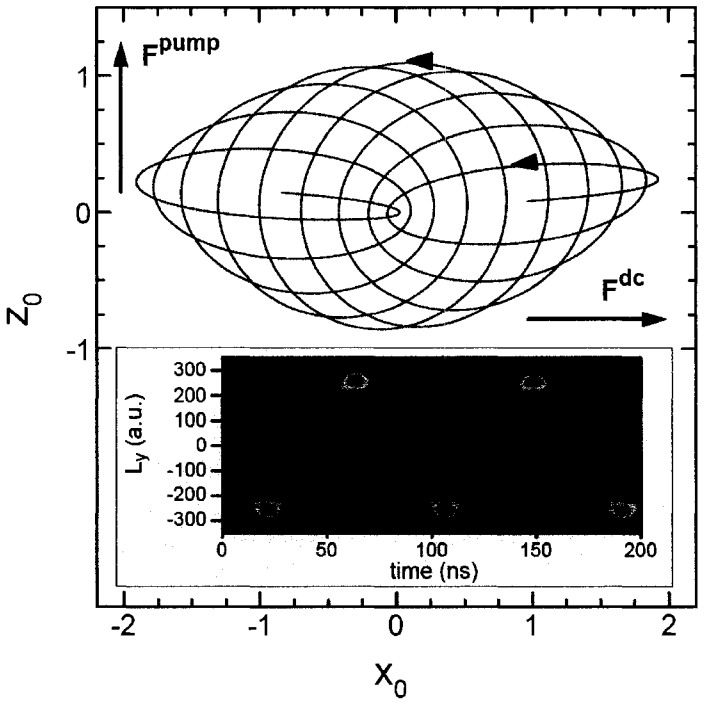

Figure 4.2 : Electron trajectory and angular momentum distribution in the presence of a -20 mV/cm electric field step. The upper portion of the figure shows an electron trajectory over a time $T_s/2$. The inset figure shows the change in the angular momentum distribution, L_y, with field step duration.

turn off the field, allowing the high L_y wavepacket to evolve freely.

The results of CTMC simulations showing the evolution of the expectation values of the components of the momentum and spatial coordinates of the wavepacket following turn-off of the field step are presented in Fig. 4.3 and Fig. 4.4. Rewriting Eqs. 1.2 and 1.3,

$$\Big(x(t), z(t)\Big) \simeq \left(n^2 \cos\Big(-\frac{2\pi t}{T_n}\Big), n^2 \sin\Big(-\frac{2\pi t}{T_n}\Big)\right). \tag{4.1}$$

$$\Big(p_x(t), p_z(t)\Big) = \left(\frac{\mathrm{d}x}{\mathrm{d}t}, \frac{\mathrm{d}z}{\mathrm{d}t}\right) = \left(\frac{1}{n}\sin\Big(-\frac{2\pi t}{T_n}\Big), -\frac{1}{n}\cos\Big(-\frac{2\pi t}{T_n}\Big)\right), \tag{4.2}$$

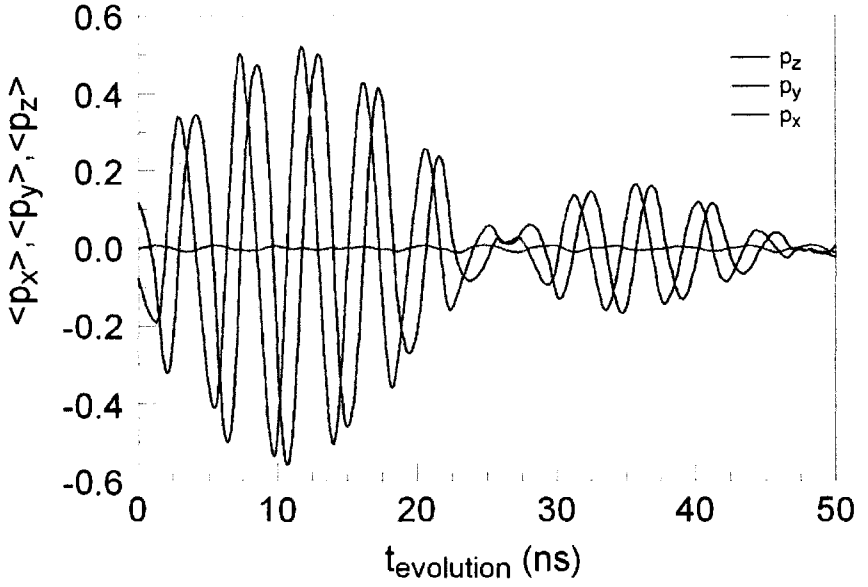

Figure 4.3 : Evolution of the expectation values of the momentum components following the termination of a -20 mV/cm field step.

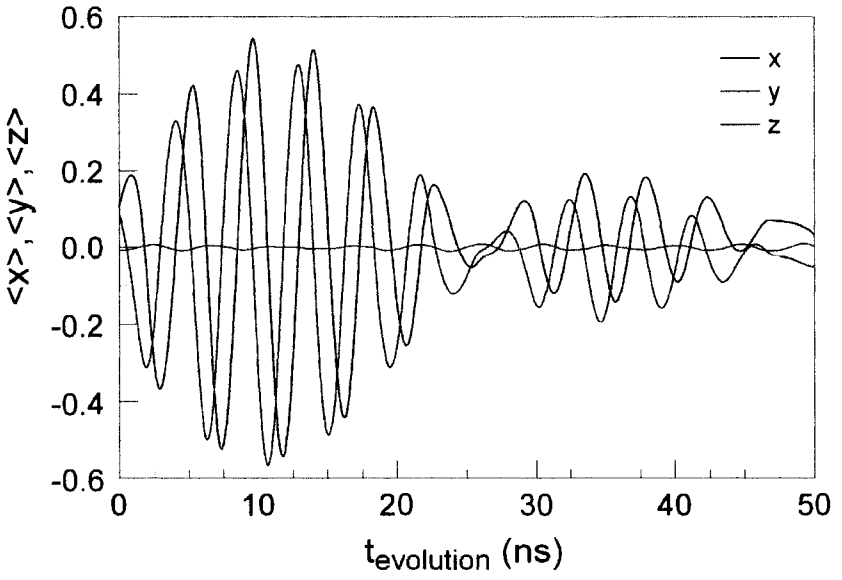

Figure 4.4 : Time dependence of the expectation values of the electron position following turn-off of the field step.

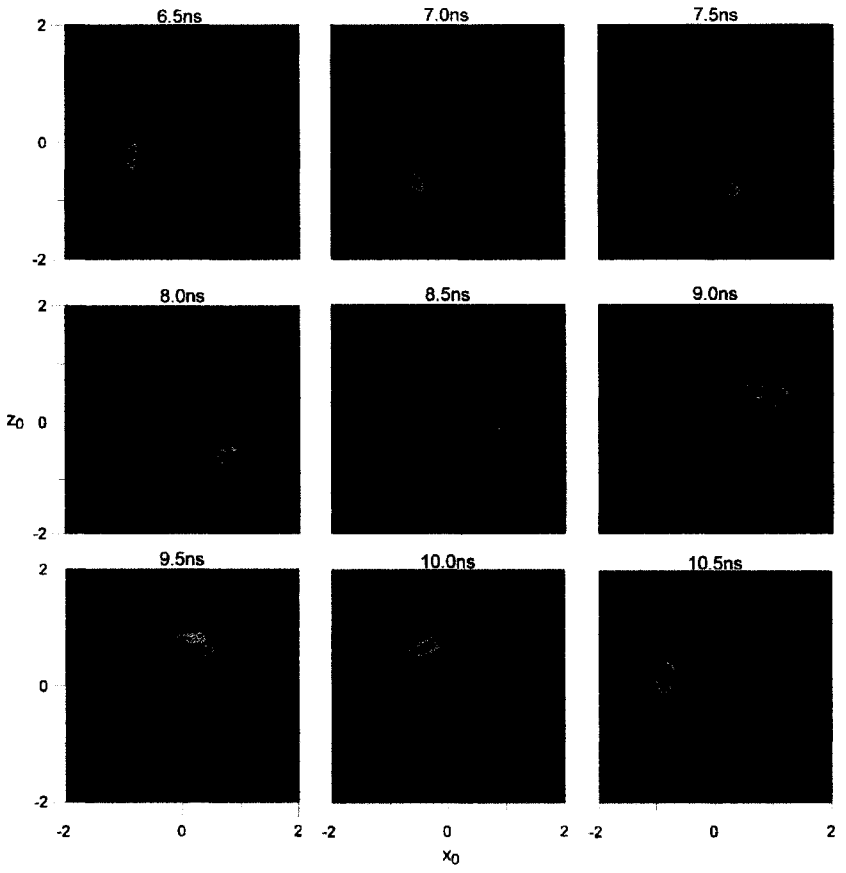

Figure 4.5 : Simulated evolution of the spatial distribution of the orbiting wavepacket with time. Times are relative to the termination of a -20 mV/cm field step. The wavepacket orbits the nucleus in a counterclockwise manner.

shows a 90° phase shift between the expectation values of the x and z coordinates, and the x and z components of momentum is expected, as is observed in the figures. Furthermore, for counterclockwise rotation the maximum $\langle x \rangle$ should coincide with the maximum in $\langle p_z \rangle$ as is also shown.

Maximum localization of the wavepacket occurs a few orbital periods after turning off the field step. The snapshots in Fig. 4.5 were taken near the time of maximum

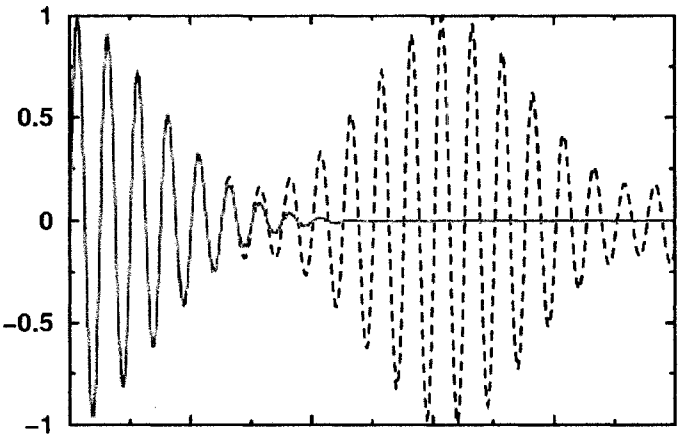

Figure 4.6 : An example of superpositions of functions with nearly identical, but continuous (blue) vs. discrete (red) frequency spectra [40].

localization, and show the counterclockwise motion of the wavepacket in the xz plane. The transient localization then decays as the wavepacket becomes more evenly distributed around the orbit.

A small revival is seen in the wavepacket localization at later times, as a result of partial rephasing. Figure 4.6 illustrates an example of the behavior of a superposition of functions with continuous (blue) vs. discrete (red) frequency spectra. Functions with discrete spectra rephase periodically, and a full revival in amplitude is seen. Continuous distributions, however, contain a dense frequency spectrum and no revivals occur. The energy level separation at $n = 306$, ~ 1 μeV, is much smaller than the binding energy, ~ 150 μeV, and revivals of successively decreasing amplitude are expected.

The CTMC simulations described in this section give a clear picture of the expected properties of the nonstationary localized circular wavepackets being studied.

The results of these simulations are used as a guide in the experimental realization of the wavepackets, discussed in the next section.

4.2 Experimental Results

The production of the wavepackets follows, exactly, the description given in the previous section. The subsequent evolution of the wavepackets was monitored using probe electric field pulses applied along the x and z axes. Because a given voltage pulse applied to the side electrode in the IR produces a field that is only 8% of that generated by applying the same pulse to the top electrode, it was not possible experimentally to monitor the evolution of the momentum components along the x-axis through the use of impulsive ionization. A longer -100 mV/cm probe pulse was therefore used, whose duration is 6 ns. Such pulses probe the spatial characteristics of the wavepacket by ionizing those electrons whose z (or x) coordinates are such that their energy, $-1/(2n^2) + zF_{probe}$, is larger than the top of the potential saddle, $-2\sqrt{|F_{probe}|}$, generated by the probe pulse [41].

Figure 4.7 shows survival probabilities measured following application of a pump field of $F^{(z)}_{pump} = -20$ mV/cm for 22 ns as a function of the time delay, t_d, between the turn-off of the pump field and application of the probe pulses. Strong periodic oscillations in the survival probabilities are evident which are in excellent agreement with the CTMC predictions. In addition, the survival probabilities well reflect the dynamical behavior of the expectation values $\langle x \rangle$ and $\langle z \rangle$ indicating that the wavepacket

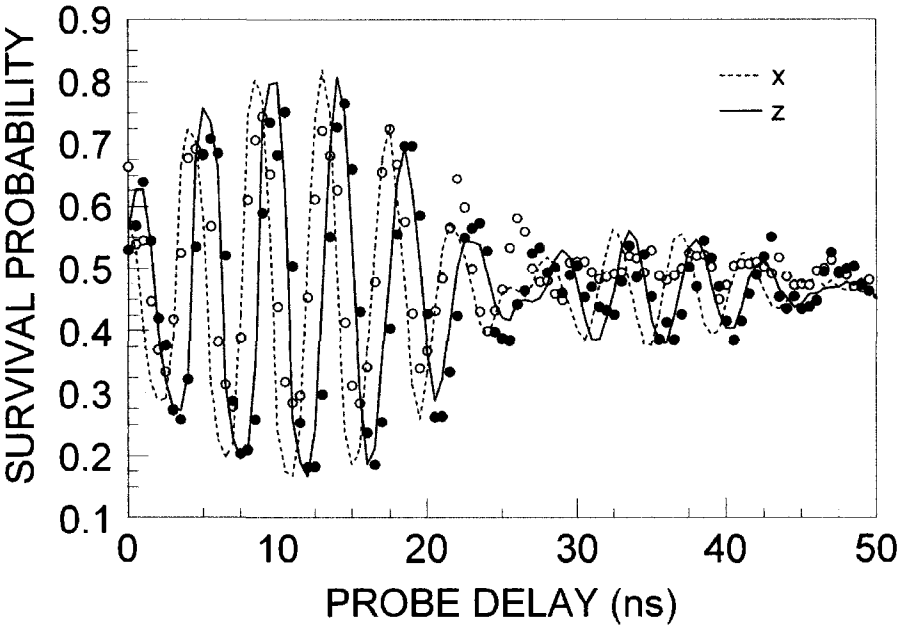

Figure 4.7 : Survival probabilities when probing in the x (blue) and z (black) directions, following a -20 mV/cm field step with 22 ns duration. The x data leads the z data by 90°, corresponding to counterclockwise motion. Circles represent experimental data, while the lines are CTMC results.

follows a circular orbit and remains localized over several periods. Evidence of a revival in localization is seen after $\sim$ 30 ns.

The results presented above were obtained by turning off the dc field at $t \sim 22$ ns to create a wavepacket orbiting counterclockwise in the xz plane, i.e., with $L_y \sim -300$. Measurements were also undertaken in which the field was turned off at $t \sim 65$ ns to form a wavepacket rotating clockwise in the xz plane, i.e., with $L_y \sim +300$. Application of probe pulses along the x and z axes revealed behavior similar to that seen in Fig. 4.7. These results are displayed in Fig. 4.8. The sign of the 90° phase shift between measurements made along the x and z axes is reversed compared to

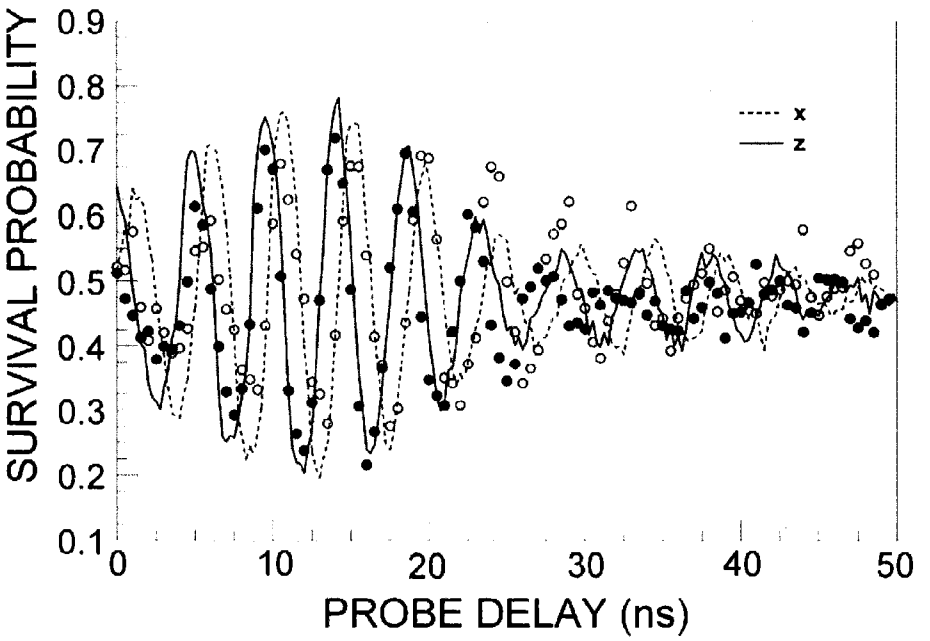

Figure 4.8 : Survival probabilities when probing in the x (blue) and z (black) directions, following a -20 mV/cm field step with 66 ns duration. The z data here leads the x data by 90°, corresponding to clockwise motion. Circles represent experimental data, while the lines are CTMC results.

Fig. 4.7, consistent with the expected opposite sense of rotation of the wavepacket. Agreement between theory and experiment is again good.

To further explore the orbital behavior, the evolution of the electron momentum was monitored using very-short HCPs with durations $T_p \sim 800$ ps $\ll T_n$. In this limit, each pulse $F_{probe}(t)$ simply delivers an impulsive momentum kick to the excited electron. When the electron is located on the $+x$ axis moving in the $+z$ direction ($t = 4$ ns in Fig. 4.9) a kick Δp in the $+z$ direction will accelerate the electron and increase its energy. Even relatively small kicks can lead to ionization. In contrast, if the electron is located on the $-x$ axis traveling in the $-z$ direction ($t = 6.4$ ns in

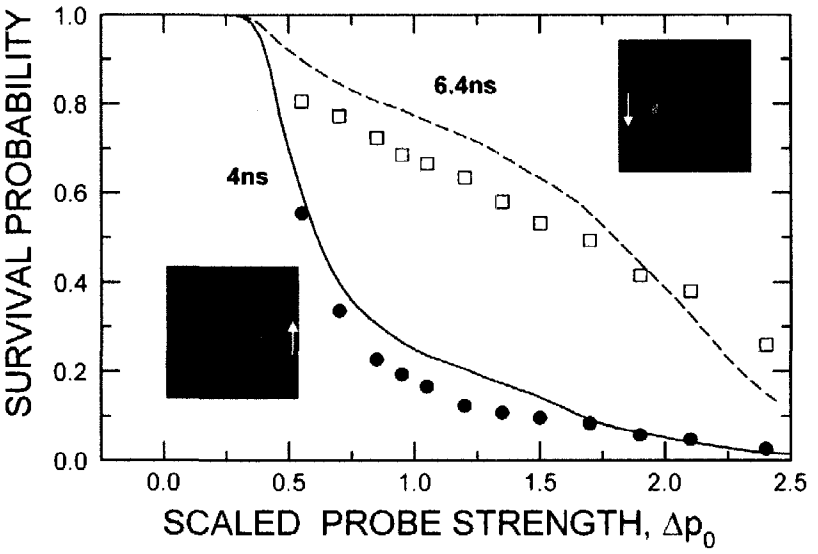

Figure 4.9 : Survival probabilities measured as a function of the strength, Δp, of a probe kick (expressed in scaled units $\Delta p_0 = np$) that is applied in the z direction when ($t = 4$ ns) the electron is located on the $+x$ axis moving in the $+z$ direction and when ($t = 6.4$ ns) it is located on the $-x$ axis moving in the $-z$ direction. Points represent experimental data, while results of CTMC simulations are represented by lines.

Fig. 4.9), small kicks will tend to decelerate the electron and reduce its electron energy leading to stronger binding. Only if the kick strength satisfies the condition $|\Delta p| > 2p_z$ does the electron gain energy, possibly leading to ionization. In consequence, much larger kicks are required to induce ionization. Survival probabilities measured under these two conditions are shown in Fig. 4.9 as a function of the strength of the probe kick. Pronounced differences in the ionization characteristics are seen that agree well with the results of CTMC simulations. The experimental results demonstrate clearly the production of Bohr-like localized Rydberg electron wavepackets, that travel around the ionic core in near circular orbits.

Chapter 5

Conclusions and Outlook

The present work demonstrates that application of carefully tailored electric field steps to quasi-1D Rydberg atoms can be used to create localized nonstationary wavepackets which travel in near-circular orbits around the nucleus. Although these wavepackets slowly dephase and lose their localization, their motion can be followed for several orbits and provides the closest analog yet achieved to the original Bohr model of the hydrogen atom.

The effects of the application of field steps of different amplitudes, such as -5, -10, and -40 mV/cm, are presently being explored. Preliminary results show extended localization lifetimes can be achieved with -5 and -10 mV/cm field steps. This results because application of the smaller field leads to a wavepacket that comprises a narrower distribution of the principal action, n, and therefore dephases less rapidly. The effects of the rise and fall times and of shape of the field step are also being examined to see if further improvements in localization and lifetime can be achieved.

The production of Bohr-like atoms in which the position of the electron wavepacket in its near-circular orbit is known provides new opportunities to study the behavior of periodically-driven atoms, i.e. atoms subject to a periodic train of kicks. A variety of dynamical phenomena similar to those seen for quasi-1D atoms are to be expected

which should depend not only on the strength and frequency of the kicks but also on their direction and phase relative to the electron orbit. Opportunities also exist for further atomic engineering by, for example, using a carefully-tailored sequence of kicks to move the electron to near-circular states of higher (or lower) n [42]. Preliminary simulations also show that a sequence of kicks may help to maintain localization of the wavepacket for extended periods.

Possible extension to study the interactions of Rydberg atoms in close proximity might also be possible. Although in the current setup the probability for creation of a Rydberg atom in a given laser pulse is much less than one, it is, in principle, possible to achieve much higher excitation probabilities using multistep excitation schemes [43]. One such technique that appears promising involves the use of an Argos 2400 infrared laser recently acquired, capable of producing $\sim$ 2 W of 2.3 to 3.9 μm radiation. This laser would excite electrons, initially excited by the CR-699 to the $n \sim 10$ range, to high-n.

Increased excitation rates make possible the study of blockade effects where the excitation of one atom forbids subsequent excitation of its neighbors due to energy level shifts associated with dipole-dipole or van der Waals interactions. More general investigation of dipole-dipole interactions can be realized by, for example, splitting the incident laser beam and, through tight focusing, creating two compact excitation volumes whose separation can be varied leading to a coupled two-dipole system with tuned interaction strength [30]. Such techniques will help to gain new insights

into dipole-dipole interactions which are crucial in quantum computing and quantum information processing.

Bibliography

[1] R. G. Hulet and D. Kleppner, *Phys. Rev. Lett.* **51**, 1430 (1983).

[2] C. H. Cheng, C. Y. Lee, and T. F. Gallagher, *Phys. Rev. Lett.* **73**, 3078 (1994).

[3] J. C. Day, T. Ehrenreich, S. B. Hansen, E. Horsdal-Pedersen, K. S. Mogensen, and K. Taulbjerg, *Phys. Rev. Lett.* **72**, 1612 (1994).

[4] J. Hare, M. Gross, and P. Goy, *Phys. Rev. Lett.* **61**, 1938 (1988).

[5] R. Lutwak, J. Holley, P.P. Chang, S. Paine, D. Kleppner, and T. Ducas, *Phys. Rev. A* **56**, 1443 (1997).

[6] D. Delande and J. C. Gay, *Europhys. Lett.* **5**, 303 (1988).

[7] S. Gleyzes, S. Kuhr, C. Guerlin, J. Bernu, S. Delglise, U. Busk Hoff, M. Brune, J.M. Raimond, S. Haroche, *Nature* **446**, 297 (2007).

[8] P. Bertet, S. Osnaghi, A. Rauschenbeutel, G. Nogues, A. Auffeves, M. Brune, J. M. Raimond and S. Haroche, *Nature* **411**, 166 (2001).

[9] M. Brune, F. Schmidt-Kaler, A. Maali, J. Dreyer, E. Hagley, J. M. Raimond, and S. Haroche, *Phys. Rev. Lett.* **76**, 1800 (1996).

[10] E. Hagley, X. Matre, G. Nogues, C. Wunderlich, M. Brune, J. M. Raimond, and S. Haroche, *Phys. Rev. Lett.* **79**, 1 (1997).

[11] M. Gross and J. Liang, *Phys. Rev. Lett.* **57**, 3160 (1986).

[12] Z. D. Gaeta, Michael Noel, and C. R. Stroud, *Phys. Rev. Lett.* **73**, 636 (1994).

[13] J. A. Yeazell and C. R. Stroud, *Phys. Rev. Lett.* **60**, 1494 (1988).

[14] C. L. Stokely, J. C. Lancaster, F. B. Dunning, D. G. Arbó, C. O. Reinhold, and J. Burgdörfer, *Phys. Rev. A* **67**, 013403 (2003).

[15] T. P. Hezel, C. E. Burkhardt, M. Ciocca, and J. J. Leventhal, *Am. J. Phys.*, **60**, 324 (1992).

[16] J. J. Mestayer, B. Wyker, J. C. Lancaster, F. B. Dunning, C. O. Reinhold, S. Yoshida, and J. Burgdörfer, "Realization of localized Bohr-like wavepackets", (submitted, 2008).

[17] M. T. Frey, F. B. Dunning, C. O. Reinhold, and J. Burgdörfer, *Phys. Rev. A.* **53**, R2929 (1996).

[18] M. T. Frey, Ph.D. Thesis, Physics & Astronomy, Rice University, (1996).

[19] H. Goldstein, C. Poole, and J. Safko, *Classical Mechanics*, 3rd ed., (Addison Wesley, New York, 2002).

[20] T. F. Gallagher, *Rydberg Atoms* (Cambridge University Press, New York, 1992).

[21] J. J. Sakurai, *Modern Quantum Mechanics* (Addison-Wesley Publishing, Reading, Massachusetts, 1994).

[22] Gordon Baym, *Lectures on Quantum Mechanics* (Westview Press, New York, 1969).

[23] H. E. White, *Introduction to Atomic Spectra*, (McGraw-Hill, New York and London, 1934).

[24] T. P. Hezel, C. E. Burkhardt, M. Ciocca and J. J. Leventhal, *Am. J. Phys.* **60**, 329 (1992).

[25] Richard Morris (Salix alba), distributed under the GNU Free Documentation License Version 1.2.

[26] W. E. Cooke and T. F. Gallagher, *Phys. Rev. A*, **17**, 1226 (1978).

[27] H. A. Bethe and E. E. Salpeter, *Quantum Mechanics of One- and Two-Electron Atoms*, (Springer-Verlag, Berlin, 1957).

[28] W. Zhao, J. C. Lancaster, F. B. Dunning, C. O. Reinhold, and J. Burgdörfer, *Phys. Rev. A*, **69**, 41401 (2004).

[29] M. T. Frey, X. Ling, B. G. Lindsay, K. A. Smith, and F. B. Dunning, *Rev. Sci. Instrum.* **64**, 3649 (1993).

[30] W. Zhao, Ph.D. Thesis, Physics & Astronomy, Rice University, (2007).

[31] H. J. Metcalf and P. van der Straten, *Laser Cooling and Trapping*, (Springer-Verlag, New York, 1999).

[32] B. G. Zollars, *CR-699-21 Single Frequency Ring Laser Alignment Manual*, (Internal Dunning Lab Documentation, Houston, TX, 1985).

[33] *Coherent CR-699 Ring Laser Manual*, (Coherent, Palo Alto, CA, 1982).

[34] B. G. Lindsay, *Superlock Manual*, (Internal Dunning Lab Documentation, Houston, TX, 1991).

[35] J. L. Hall and S. A. Lee, *Appl. Phys. Lett* **29**, 367 (1976).

[36] *Wavetrain Tunable CW Frequency Doubler User Manual*, Version 3.2, (Spectra-Physics GmbH, Berlin, 1999).

[37] R. W. Drever, J. L. Hall, et al., *Appl. Phys. B* **31**, 97 (1983).

[38] *KBL 25RS Product Documentation*, (Sjuts Optotechnik GmbH, Göttingen).

[39] R. F. Stebbings and F. B. Dunning, eds., *Rydberg States of Atoms and Molecules*, (Cambridge, London, 1983).

[40] S. Yoshida, Habilitationsschrift, Institute for Theoretical Physics, Technischen Universität Wien, Vienna, Austria (2007).

[41] B. E. Tannian, C. L. Stokely, F. B. Dunning, C. O. Reinhold, and J. Burgdörfer, *Phys. Rev. A*, **64**, 021404 (2001).

[42] J. J. Mestayer, W. Zhao, J. C. Lancaster, F. B. Dunning, C. O. Reinhold, S. Yoshida, and J. Burgdörfer, *Phys. Rev. Lett.*, **99**, 183003 (2007).

[43] F. B. Dunning, *Studies Involving Atoms in High Rydberg States*, NSF Grant Proposal PHY0353424.

[44] S. Yoshida, C. O. Reinhold, J. Burgdörfer, W. Zhao, J. J. Mestayer, J. C. Lancaster, and F. B. Dunning, *Phys. Rev. Lett.*, **98**, 203004 (2007).

Appendix A

Units

A.1 Atomic Units

The system of atomic units, particularly useful when considering atoms and electrons, is used in the current work. Each of the following is equal to one in atomic units:

Angular Momentum	Planck's Constant, $\hbar$	1.055×10^{-34} J s
Charge	Electron Charge, q	1.602×10^{-19} C
Mass	Electron Mass, m_e	9.109×10^{-31} kg
Length	Bohr Radius, a_0	5.292×10^{-11} m
Energy	Hartree Energy, E_h	4.360×10^{-18} J $= 27.2$ eV
Time	$\frac{\hbar}{E_h}$	2.419×10^{-17} s
Coulomb's Constant	$\frac{1}{4\pi\epsilon_0}$	8.988×10^{9} Nm^2/C^2

A.2 Scaled Units

The following scaled units are used in the current work:

$$\begin{aligned}
\vec{r_0} &= \frac{\vec{r}}{n^2} \\
\vec{p_0} &= n\vec{p} \\
t_0 &= \frac{t}{2\pi n^3} \\
\omega_0 &= n^3\omega \\
E_0 &= n^2 E \\
F_0 &= n^4 F
\end{aligned}$$